Operando Investigation of Nanocrystal based Device Energy Landscape: Seeing the Current Pathway

Mariarosa Cavallo, Dario Mastrippolito, Erwan Bossavit, Leonardo Curti, Adrien Khalili, Huichen Zhang, Nicolas Ledos, Yoann Prado, Erwan Dandeu, Michael Rosticher, et al.

Operando Investigation of Nanocrystal based Device Energy Landscape: Seeing the Current Pathway

Mariarosa Cavallo[1], Dario Mastrippolito[1], Erwan Bossavit[1], Leonardo Curti[2], Adrien Khalili[1], Huichen Zhang[1], Nicolas Ledos[1], Yoann Prado[1], Erwan Dandeu[1], Michael Rosticher[3], Sandrine Ithurria[2], Pavel Dudin[4], José Avila[4*], Debora Pierucci[1], Emmanuel Lhuillier[1*]

[1] Sorbonne Université, CNRS, Institut des NanoSciences de Paris, 4 place Jussieu, 75005 Paris, France.
[2] Laboratoire de Physique et d'Etude des Matériaux, ESPCI, PSL Research University, Sorbonne Université, CNRS, 10 rue Vauquelin, 75005 Paris, France.
[3] Laboratoire de physique de l'Ecole Normale Supérieure, ENS, Université PSL, CNRS, Sorbonne Université, Université Paris Cité, 24 Rue Lhomond, 75005 Paris, France
[4] Synchrotron SOLEIL, L'Orme des Merisiers, Départementale 128, 91190 Saint-Aubin, France.

Abstract: Due to their unique optical properties, colloidal nanocrystals (NCs) have transitioned from a solution processable luminescent liquid to an established building block for optoelectronics. As devices get more advanced, a higher degree of refinement is also required for the probe used to investigate their electronic structure. For long, device optimization has relied on the measurement of physical properties of the pristine material assuming that the latter were maintained after device integration. However, such an assumption neglects the realistic dielectric environment and possibly applied electric fields to drive the device. Hence, tools compatible with *operando* investigation of the electronic structure are required. Here, we review and present additional results relative to the *operando* investigation of infrared NCs using photoemission microscopy. This technique combines the advantages of photoemission to unveil band alignment with a sub-µm spatial resolution that is used to correlate energy shift to device geometry. This method gives direct access to parameters such as diode built-in potential, transistor lever arm or even the vectorial distribution of the electric field that are otherwise only attainable through indirect method involving modelling. We provide indications and precautions to be used in the design of devices to permit the operando analysis *via* photoemission techniques. It is, therefore, a very promising tool for the optimization of NC-based devices.

Keywords: nanocrystals, device, photoemission, microscopy, electric field, field effect transistor.

*To whom correspondence should be sent: el@insp.upmc.fr, jose.avila@synchrotron-soleil.fr

INTRODUCTION

Colloidal nanocrystals (NCs) are increasingly finding applications, spanning from light source for display [1] to single photon source for quantum optics [2–4] or infrared imaging [5,6]. Spectroscopic tools appear as a crucial bridge to transition from the material growth to the device through rational optimization. In the context of NCs, optical spectroscopy tools, that can either be static or time resolved, appear as the methods of choice to probe the density of state of the confined semiconducting nanoparticles. However, since optical methods rely on transitions between an occupied and an unoccupied state, they appear insensitive to the absolute energy of the involved states, while it is a central element for device integration. Careful design of contacts in optoelectronic devices relies on the matching between a metal work function and the energy of the bands. For NCs, absolute energy of the states can be unveiled using scanning tunnelling microscopy (STM) [7], electron microscopy coupled with spectroscopy technics such as EELS (electron energy loss spectroscopy [8–11], electrochemistry [12–14] or photoemission [15,16]. While STM and EELS offer the advantage of high spatial resolution below nanometers, the size rangethat can be probed appears too limited for operando analysis of a device, since a size range of the order of 1-100 µm is required. Electrochemistry and photoemission, on the other hand, are more macroscopic methods that have yelded significant results, particularly through the systematic study of dipoles associated with NC capping ligands and their impact on band alignment [13–15]. This has been used to design *p*-*n* junctions for solar cell applications [17]. Furthermore, these two methods present fewer constrains on the substrate compared to TEM, which requires thin samples that may not be representative of traditional device design. However, the potential of photoemission extends beyond only revealing band alignment and analysing the chemical environment.

In the context of optimizing optoelectronic devices based on NCs, several advanced photoemission techniques have been employed. Initially, an in-depth analysis is facilitated through the utilization of an energy-tunable synchrotron source [18]. Subsequently, time-resolved pump-probe measurements have been exploited to identify the nature of the majority carrier [19], or the coupling between optically active layer and charge transport layers [20–22]. Here, our focus lies on exploring the potential of photoemission microscopy as *in-situ* probe for mapping the energy landscape of a device during operation (i.e., *operando* measurements). Such method allows to account for the realistic dielectric environment of nanocrystals and includes the effect of electric and electromagnetic fields.

Here, we begin by reviewing the specifics and requirements of the method, before applying it to obtain a complete 3D reconstruction of the energy landscape in a field-effect transistor under drain and gate bias. Beyond scalar information, the high spatial resolution of the method gives access to the vectorial distribution of the electric field, thus revealing the current flow path in a NC film. The last part of the paper reviews some of the recent applications of the method to the design of NC-based optoelectronic devices.

Photoemission microscopy

Conventional X-ray photoemission is a spectroscopic method where UV or X-ray beam is shone on the sample with a photon energy *hv* (with *h* the Planck constant and *v* the photon frequency) chosen based on the work function or the core level energy to be probed. This allows for photoelectrons to escape from the sample and get collected in an electron analyzer to measure their kinetic energy (KE). If the electron only experiences elastic scattering, energy conversion ensures that $hv=BE+KE+W_{Fa}$, with W_{Fa} being the work function of the analyzer and BE the binding energy. The

binding energy is a material parameter in this equation and contains information about the chemical environment of the electron.

Expanding the X-ray photoemission experiment from spectroscopy to spectro-microscopy becomes feasible when we not only measure the kinetic energy of the photoelectron but also accurately determine the point of origin for each emitted electron. This methodology is employed in a Photoemission Electron Microscope (PEEM). The operating principle of a PEEM is comparable to that of an optical microscope. However, instead of imaging and magnifying visible light, a PEEM captures and visualizes the lateral intensity distribution of photoelectrons using magnetic or electrostatic lenses. The mechanisms responsible for lateral intensity variations within the image are highly dependent on both the excitation light source and the sample characteristics. When an UV light source is used, like Hg or He discharge lamps, the photon energy of the excitation light is close to the ionization threshold of the material, then PEEM contrast can result from variations in work function on the sample surface. If we combine PEEM with a variable *hv* (as in a synchrotron facility) and an energy-filtering element, such as a hemispherical analyzer, the detection of the kinetic energy of core-level electrons becomes possible, enabling spatially resolved chemical analysis. These instruments are commonly referred to as energy-filtered PEEM (EF-PEEM or XPEEM).

Table 1 Spatially resolved photoemission methods and comparison of their spatial and energetic resolutions

Spatially resolved photoemission method	**Lateral resolution (nm)**	**Energy resolution (meV)**	**Comment**	**References**
PEEM+UV source	20-100	150-500	Secondary electron no chemical contrast	[23,24]
PEEM + X-ray source (XPEEM)	500-1000	500		[23,25]
PEEM + synchrotron X-ray source (XPEEM)	20-150	50-800	Lateral and energy resolutions depend on the type of instruments (manufacturer, magnetic or electrostatic lenses, etc.) and on beamline specifications.	[23,24,26–33]
Nano focused scanning photoemission microscopy (SPEM)	100-700 nm (here)	30 meV @300 K 15 meV @80 K		[34–45]

Using this approach, spatial resolutions as fine as tens of nm have been achieved (Table 1). When applied to NCs, there is reason to hope that information on nearly individual particle can be obtained.

However, there is a trade-off to be found between the spatial and the energy resolution. *Operando* investigation also requires a higher energy resolution such as the one required by conventional chemical mapping. Moreover, a specific limitation in PEEM experiments arises from the requirement for high voltage between the sample and the objective lens of the microscope in order to achieve high-resolution imaging. This voltage can be up to 20 kV (30 kV for hard X-ray PEEM - HAXPEEM) [46], especially when the high spatial resolution is required. Therefore, having a clean and smooth surface becomes essential, since the high extractor field associated with this voltage can induce discharges between the sample and the optics. These discharges not only reduce spatial resolution but can also potentially damage both sample and instrument. This concern is particularly crucial for *operando* measurements, where it can seriously affect device contacts.

A complementary approach to PEEM for achieving high spatial resolution in imaging emitted photoelectrons involves employing suitable photon optics to reduce the magnification of the photon beam and focus it onto a spot with sub-micrometer dimensions on the sample. This focusing can be obtained using a Fresnel zone plate (FZP), a Schwarzschild objective or a capillary mirror [41–45], see **Figure 1**a. However, this increased focus comes at the cost of a significant reduction in incident flux, especially in the case of FZP, making the method applicable primarily with synchrotron beams. The spot size is determined by photon optics but also by the monochromaticity of the beamline, requiring high quality X-ray optics upfront the experiment (i.e., Kirkpatrick–Baez mirrors or Wolter mirror). Depending on the beamline configuration and design, spot sizes as small as 100 nm can be achieved [38–40]. This length scale makes the method well suited to probe semiconductor devices that are few µm in size and being also substrate compatible. It, on the other hand, averages all details relative to single NC charge distribution that will require combination of method (STM or TEM based with higher spatial resolution) to generate a complete image of the electronic structure.

By combining this setup with a high energy resolution hemispherical analyzer, resolutions down to 15 meV can be reached [47–49]. When this highly focused X-ray beam is coupled with a raster scan of the sample by fine movements of the sample stage, a microscopic image of the sample can be generated. A photoemission spectrum is acquired for each point, so the lateral resolution is primarily determined by the size of the X-ray beam spot. This technique, known as scanning photoemission microscopy (SPEM), offers the advantage of achieving sub-micrometric resolution without the need for applying high voltage, thus eliminating all the associated risks mentioned earlier. The data presented here were acquired at the ANTARES beamline (synchrotron SOLEIL) using a FZP to focus the initial 2.5-3 mm wide X-ray beam to approximately 700 nm. As Fresnel lenses are chromatic tools, they are designed for a specific energy range. In this particular case, the design corresponds to the soft X-ray window around 100 eV ($h\nu$ = 95 eV was used for the presented data). This can represent a constraint on possible core levels that might be investigated. However, this limitation has to be mitigated since most materials used for nanocrystals display a photoemission peak at low binding energy (BE) (BE(Cd 4d)≈10 eV, BE(Ag 4p)≈57 eV, BE(In 4d)≈17 eV, BE (As 3d) ≈41 eV; BE(Cu 3p)≈76 eV, BE(Hg 5d)≈8 eV, BE(Pb 5d)≈18 eV …). Those low energy states may nevertheless have a limited cross section [50,51] which further supports the use of high-intensity sources. Here, we focus on two materials that are HgTe [52–54] (**Figure 1**b-c and S1) and PbS (Figures S4-S5), two narrow band gap materials that have led to the most advanced developments for infrared optoelectronics based on NCs, with demonstration of infrared imagers [5,6,55–58], light emitting diodes and advanced coupling with photonics structure [59,60].

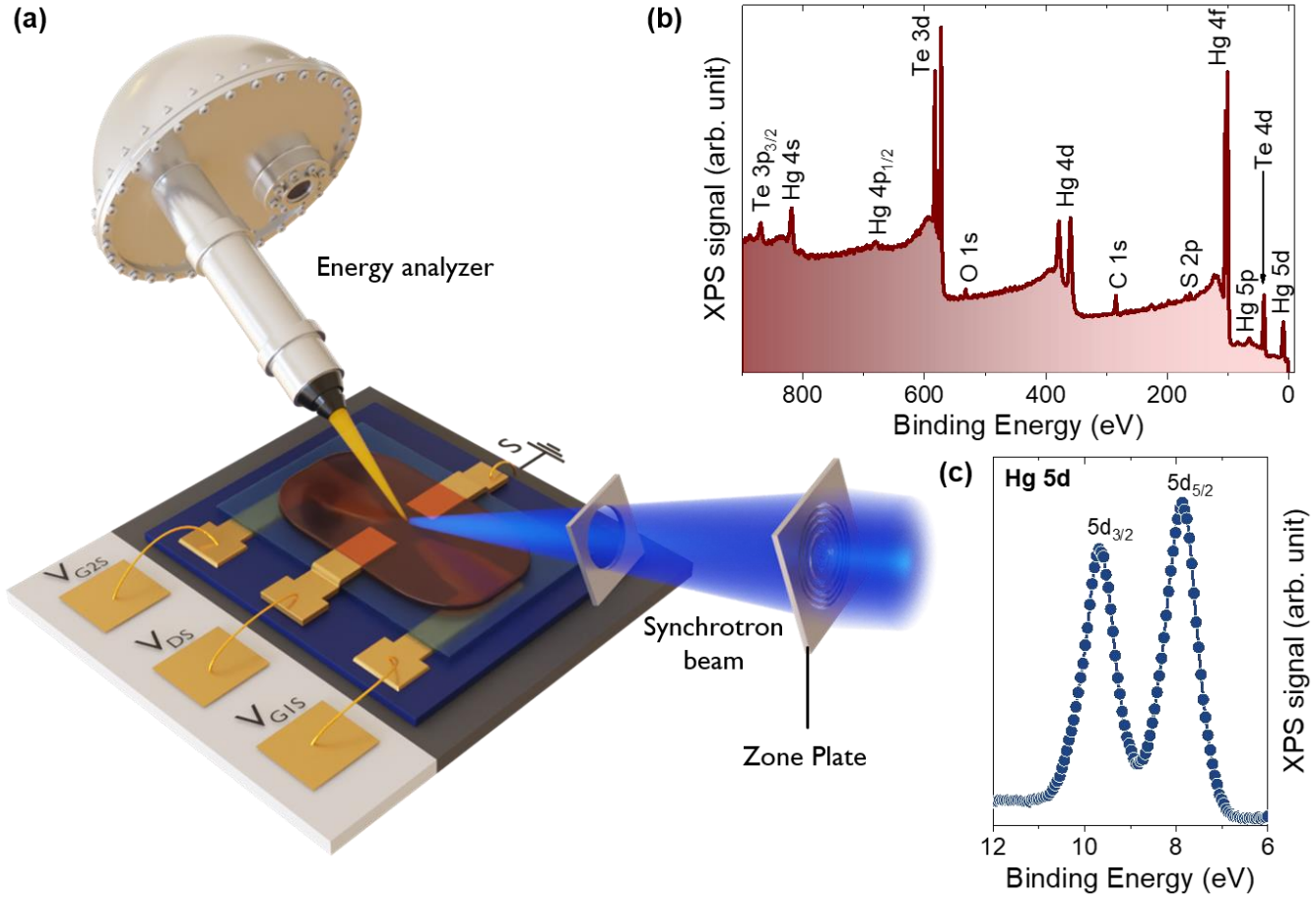

Figure 1 Photoemission microscopy*. a Schematic of the X-ray photoemission microscopy setup in which a focused soft X-ray beam is used to illuminate the sample under operation and emitted electrons are probed by the electron analyzer. b. Survey photoemission spectrum from a HgTe NCs thin film. c. Photoemission from the Hg 5d state from the same film as part b.*

Requirement on samples

Photoemission, being a surface sensitive method, only allows to probe the top layer. With a photon energy of 95 eV, the photoelectron escape depth is limited to approximately 1 nm [61,62]. Minimizing sample charging is also crucial and relates to device geometry: large scale device (several tens of µm) fabricated on an insulating substrate will inevitably lead to the accumulation of positive charges. This charge accumulation brings an electrostatic shift of the photoemission spectrum, possibly over a range (tens of eV) much larger than the applied biases. Therefore, better results have been obtained while a metallic plane is implemented below the active area with a limited electrode spacing. Another important aspect is the conductivity of the NC film itself. To facilitate the injection of carriers by the electrode while preserving charge neutrality, it is crucial to render the film conductive through a ligand exchange step. This step is advantageous, especially in the context of *operando* measurements, as it allows for the preparation of the film in a similar manner for both the device and the photoemission experiment. Additionally, it's important to point out that the sign of the applied bias is generally chosen to minimize the charging effect.

While for transport the localization of the electrodes is mostly driven by spatial considerations, photoemission imposes an additional constraint. In this case, it is essential to position the electrodes and their associated wiring away from the photoelectrons path to prevent the bias application from deflecting the photoelectron on its way to the analyzer.

Here, we focus on a field effect transistor geometry (FET), whose fabrication steps are depicted in **Figure 2**a to d. Compared to conventional configurations where the gate is located between the drain and source electrodes, we opted for two geometries which better evidence the impact of each type of electrode. A dual gated FET (**Figure 2**e-f) is used to mimic *p-n* junction, while opposite biases are applied on the two gates. The geometry of the single gate device (**Figure 2**g) is chosen to see how the electric field lines and associated current flow get modified by the gate potential.

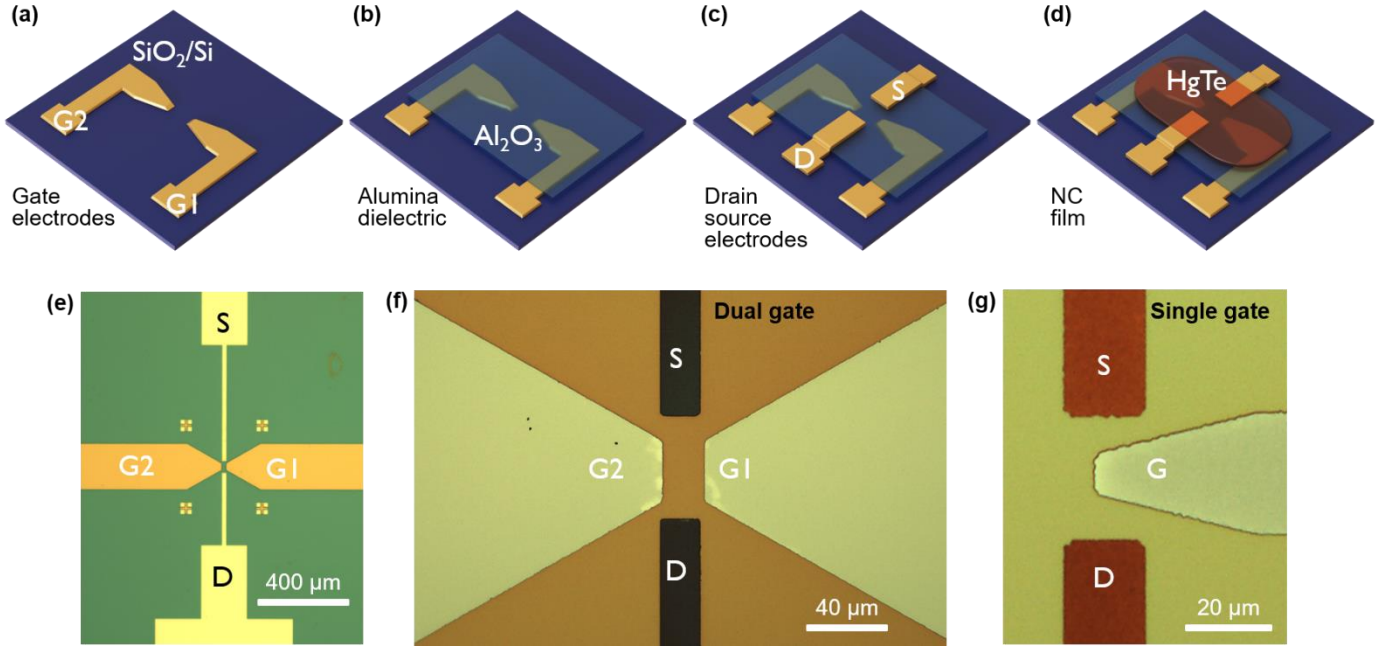

Figure 2 Gated nanocrystal film fabrication*. Parts a to d depict the main fabrication setup relying on conventional optical lithography setup and atomic layer deposition. e. Optical microscopy image of the dual gated FET before the deposition of the NC film. f. (resp. g.) Optical microscopy image of the dual (resp. single) gated FET after the deposition of the NC film.*

Operando mapping of the energy landscape

For a given bias configuration (set of drain and gate bias), the sample is spatially scanned under the beam. For each position, a core level spectrum is acquired. We then tracked how the binding energy of the probed state spatially shifts. A complete description of the procedure is described in Figure S2. In brief, a Gaussian fit is applied to each spectrum to determine the peak energy. The energy mean value for this Gaussian is then plotted on a map as shown in **Figure 3**a.

As a rigid shift is expected between the core level and the valence band, this map directly reflects the valence band profile. In such map, the contrast between the source and drain relates to the drain source bias, while the opposite color over the area corresponding to the two gates reflects the opposite sign of the applied bias.

A clearer picture of the device energy landscape is depicted by plotting a 3D map of the energy shift. This shift is defined as the difference between the map while bias(es) is (are) applied with respect to the grounded map. This procedure enables to account for possible remaining charging effect. An example of such 3D mapping is given in **Figure 3**b for similar biases on both gates and **Figure 3**c for opposite biases. Here, the reported data are given for HgTe NCs, but to demonstrate the generality of the method, similar maps obtained for PbS NCs are given in Figure S5.

From this map, we directly quantify the gate lever arm, denoted as α, which represents the energy shift (ΔBE) per unit of gate bias (ΔV_G). This parameter, $\alpha=\Delta BE/\Delta V_G$, is also equivalent to the ratio of the gate capacitance over the total capacitance [63–65] of the combination of the gate and the NC film. A linear fit of the graph ΔBE vs V_G (**Figure 3**d) leads to $\alpha=0.15$ eV·V^{-1}. In other words, this implies that a 6 V gate bias is needed to induce a 1 eV displacement. This limited efficiency indicates that part of the charge is used to passivate the dielectric dangling bonds or leaks in the NC film. A second important output of the graph is that a shift larger than the band gap appears, suggesting the potential for degenerate doping and the emergence of associated intraband transitions. A previous study by Cavallo *et al.* has demonstrated that the decay length for the amplitude of the gate induced shift is around 75 nm [34], see **Figure 3**e, meaning that efficient gating can be obtained even for films which are 100-200 nm thick. Such reasonably large thickness justifies *a posteriori* the design of phototransistor [66–71] based on surface gating method (i.e. dielectric or ferroelectric as opposed to electrolyte) that can combine at the same time reasonable absorption with tunability of the current through the gate effect.

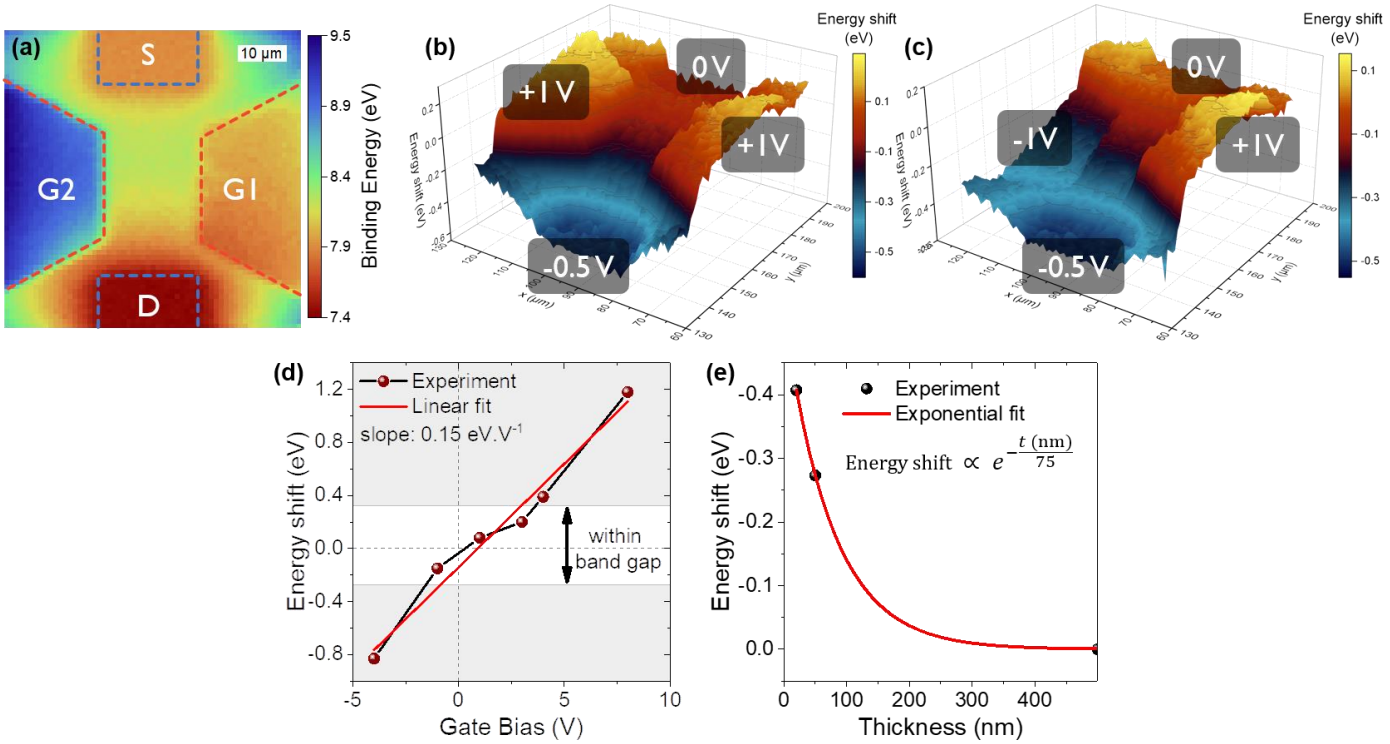

Figure 3 Operando 3D mapping of the FET energy landscape with HgTe NCs channel*. a. Binding energy map of the Hg 5d$_{5/2}$ state for the dual gated FET while V_{DS}=-0.5 V, V_{G2S}=+4 V and V_{G1S}=-4 V, data are acquired at 240 K. b. (resp c.) 3D mapping of the energy shift (reference is taken with all electrodes grounded) while V_{DS}=-0.5 V, V_{G2S}=+1 V and V_{G1S}=+1 V, (resp V_{DS}=-0.5 V, V_{G2S}=-1 V and V_{G1S}=+1 V). d. Energy shift induced by gate as a function of the applied gate bias. The red line corresponds to a linear fit and enables lever arm determination which is found to be 0.15 eV·V^{-1}.e. Gate induced energy shift as a function of the film thickness. Part e is adapted with permission from ref [34]. Copyright (2023) American Chemical Society.*

With the second electrodes geometry (**Figure 2**g), where the gate is localized in the middle of the source-drain channel (**Figure 4**a-c), we can easily observe the possibility of using the gate electrode to either define the attractive area for the electrons or conversely, form a barrier (**Figure 4**b). Thanks to the high spatial resolution of the method, we can then further observe the shaping of the vectorial electric field map by the gate. As $\vec{F} = -\vec{\nabla}V$, where V is the electric potential, one can directly relate

the experimental data through $\vec{F} = -\nabla(\Delta BE) = -\frac{\partial \Delta BE}{\partial x}\hat{x} - \frac{\partial \Delta BE}{\partial y}\hat{y}$, where ΔBE is the measured binding energy shift. Furthermore, since in a drift model the local current is expected to follow the electric field magnitude, this mapping is actually a representative image of the local drift current.

We can then superimpose the energy shift map with the vectorial map as proposed in **Figure 4**d-e for two different gate bias configurations and Figure S3 for the dual gated FET. In the absence of gate bias, the electric field distribution resembles the behavior expected for a dipole, see **Figure 4**d. The application of gate bias affects this distribution, and more strikingly at the edge of the electrodes.

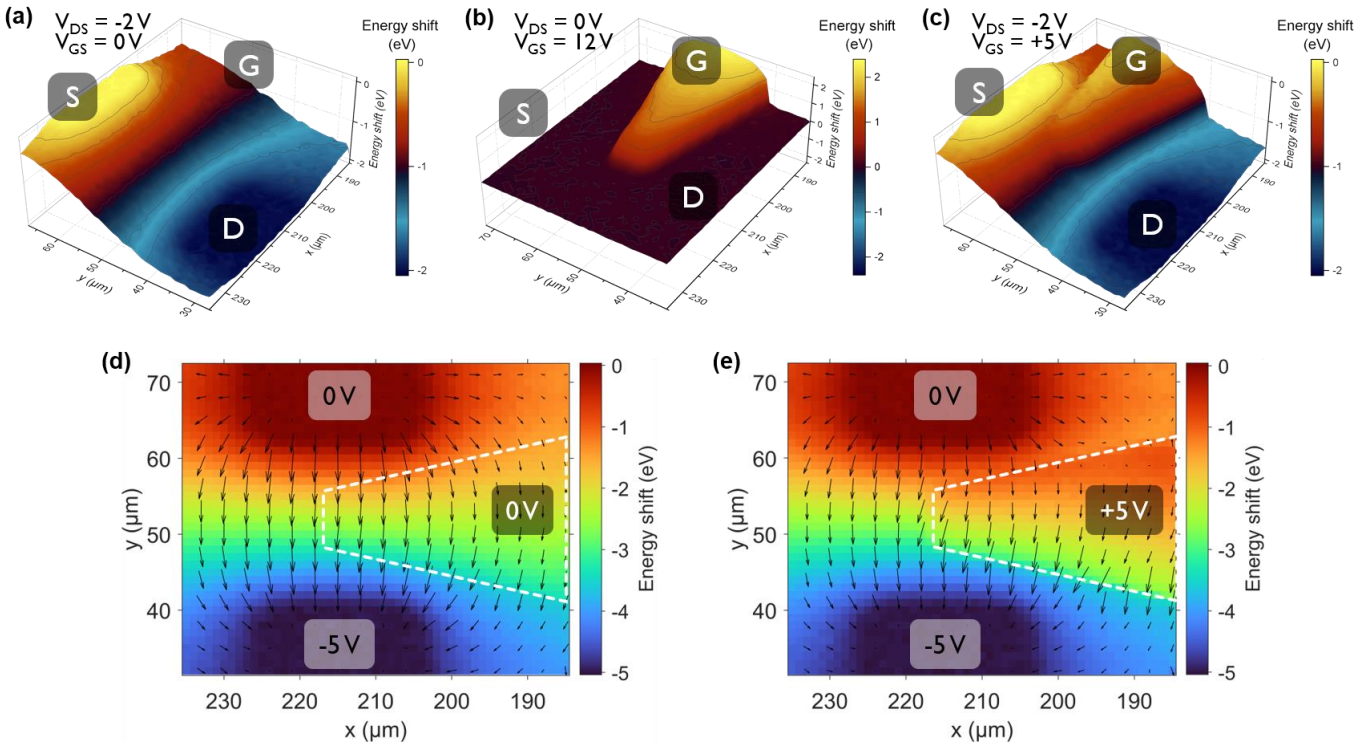

***Figure 4 Seeing the current flow**. a, b and c are respectively energy shift maps for the single gated device for V_{DS}=-2 V, V_{GS}=0 V ; V_{DS}=0 V, V_{GS}=+12 V and V_{DS}=-2 V, V_{GS}=+5 V . d (resp e.) are superposition of the energy shift map (color map) and electric field map in which the field direction and magnitude are given by the arrow for each position, while V_{DS}=-5 V and V_{GS}=0 V (resp. V_{GS}=+5 V)*

Exploring various device geometries

Now that the method is established and its potential as a probe of the NC based energy landscape demonstrated, we would like to review some of the recent results where this method has been used to unveil properties of optoelectronic devices. Microscopy photoemission appears as a promising tool to probe a diode's built-in potential [37,72,73]. The built-in potential from the diode is an important parameter that determines the efficiency of charge dissociation. The general route to access it relies on transport measurement under illumination, with the IV curves displaying a non-null bias under zero current, the open circuit voltage, from which extrapolation to null temperature connects to the built-in potential. However, the method is not straightforward and relies on extrapolation. With photoemission microscopy, it is possible to directly determine this potential with only a minor geometrical update [37]. This is because, as explained earlier, the probed layer needs to be on top. Thus, instead of building a conventional vertical stack, a planar version of the stack has been proposed [37,72,73], see Figure S4. A sketch for one of them is proposed in **Figure 5**a.

The planar diode is built on a metallic layer to minimize sample charging. The latter is functionalized with a given transport layer (here SnO_2 acting as the electron transport layer [74]), while the transport layer for the complementary charge is made by patterning the first layer. Here Ag_2Te is used as the hole transport layer [75]. These two transport layers induced remote doping in the top capping layer made of HgTe NCs. This effect can be directly mapped through the binding energy shift of a core level from the active layer, here, again the Hg $5d_{5/2}$ state, see **Figure 5**b. It is worth pointing out that, despite the complex composition of the sample, X-ray photoemission, through the analysis of the core level, allows the specific tracking of a given layer. The mapping of the core level binding energy unveils a shift toward higher binding energy (**Figure 5**c) when the semiconductor overlaps with the electron transport layer, which matches the expected behavior for a *n*-type material. The binding energy shift is on the order of 115 meV, which requires a high-resolution photoemission method to be accurately determined, see **Table 1**. The measured built-in potential corresponds to ¼ of the semiconductor band gap, suggesting that future effort has to be focused on surface passivation to reduce traps and then increasing the magnitude of remote doping. A similar work has also been conducted for PbS NCs [73], this time using a TiO_2/PbS/NiO planar diode. It has been observed that the built-in potential drops faster than the band gap as the latter is reduced using larger NCs with band edges ranging from 1000 to 1550 nm. This behavior has been connected to the change in doping of the sample, transitioning from quasi-intrinsic for the smallest particles to a strong n-doping for the largest.

Investigation of the remote doping can be further extended to the coupling of ferroelectric with NCs. The polarization of a ferroelectric can act as a static gate, and depending on its sign, it will affect the carrier density of the covering semiconductor. This concept has been exploited using PZT ($PbZrTiO_3$) as ferroelectric and HgTe as semiconductor, see **Figure 5**d and S4. Prior to the NC deposition the domain of the PZT has been oriented using piezoforce microscopy, in which a polarized AFM tip induces an orientation for the ferroelectric material, see **Figure 5**e. Then using photoemission microscopy, we can map how the domain orientation impacts the binding energy of the coating semiconductor. A complete correlation is obtained for the piezoresponse (polarization of the ferroelectric) and the semiconductor binding energy, see **Figure 5**f.

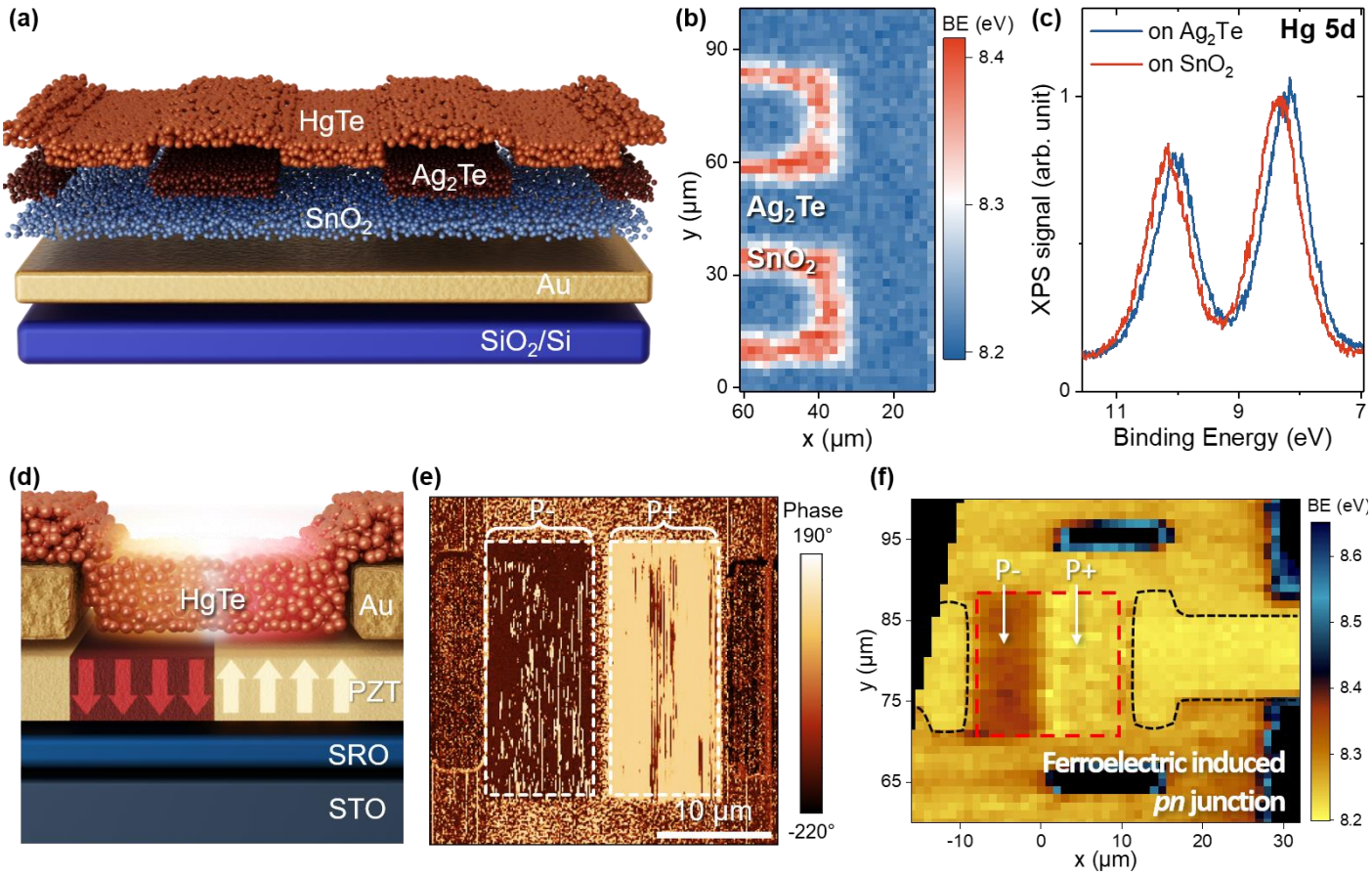

Figure 5 Application to the investigation of photodiode electronic structure*. a. Schematic of an infrared photodiode, that has been planarized to make its investigation through photoemission possible. b. Binding energy map of the Hg $5d_{5/2}$ state from a HgTe NCs film over a SnO_2 (n-type layer) substrate covered by an Ag_2Te (p-type layer) interdigiated pattern. c. Photoemission spectra for the Hg 5d state atop the SnO_2 substrate or atop Ag_2Te layer. Parts a to c are adapted with permission from ref [37]. RSC (2023). d. Schematic of ferroelectric domain coupled to a film of HgTe NCs. e. Piezoforce microscopy image showing an upward and a downward domain of PZT. f. Binding energy map for the Hg $5d_{5/2}$ state over the two domains defined in part e. Parts d to f are adapted with permission from ref [35]. Copyright (2023) Wiley.*

Beyond scalar mapping

The benefit of the method has been extended to the vectorial mapping of the electric field in the context of infrared imager. In this case, the structure of interest mimics the pixel on the surface of a read-out integrated circuit (ROIC) [76], see **Figure 6**a. The question of interest, in that case, was the determination of the actual active area between the electrodes. In a FET configuration, the two electrodes are designed to face each other, creating a homogeneous electric field. On the surface of a ROIC, the current lines may acquire a complex distribution, and the optical mode needs to be spatially matched to where the current is located. Here, the map (**Figure 6**b) allows quantifying how much of the field lines remain important even at distances where lateral transport gets involved. It is also interesting to point out that the electric field distribution points toward a maximum of the field magnitude away from the electrode. In this sense, the charges generated further away from the electrode, and consequently less likely to be collected, benefit from an advantage compared to the charges generated closer, which only experience a reduced electric field.

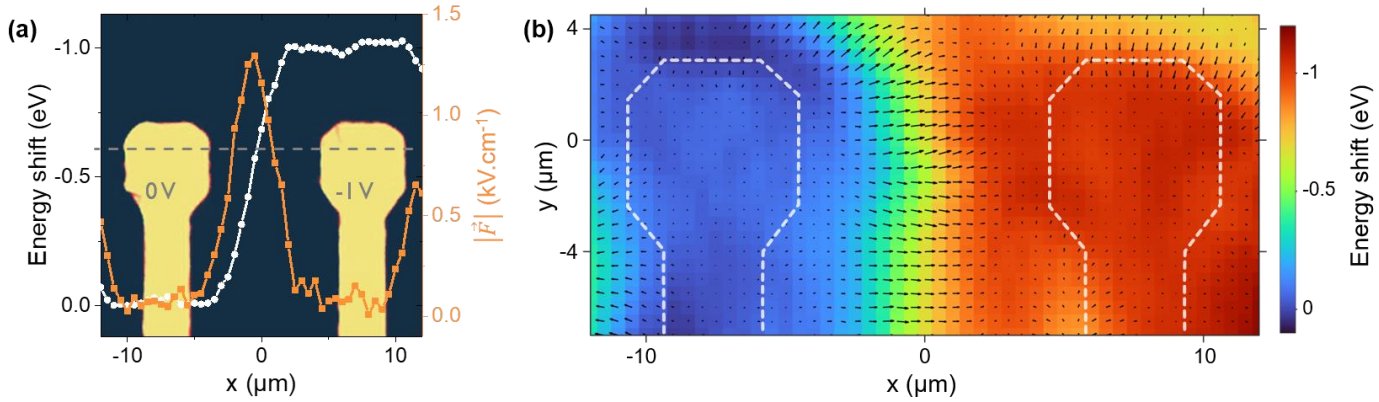

Figure 6 Scalar and vectorial of binding energy in pixel like structure*. a. Energy shift and magnitude of the electric field over a two electrodes structure depicted by the image in background. b. Energy shift map and vectorial electric field map while 1 V is applied over the two pixels. Parts a and b are adapted with permission from ref [76]. Copyright (2023) American Chemical Society.*

To conclude, the high spatial and energetic resolution of nanobeam photoemission beamlines appears as a well-suited tool to probe the energy landscape of nanocrystal-based device. It enables *operando* measurements and gives access to parameters such as the transistor lever arm and the diode built-in potential, which are otherwise difficult to access. This tool proves invaluable for device optimization. Future effort should be focused on enhancing the spatial resolution. For instance, to accurately determine the Schottky barrier, whose spatial extension typically falls within the range of tens of nm for typical doping in NCs film. Another interesting development would involve using tools that operate at higher photon energy to increase the photoelectron escape depth (i.e. HAXPES setup). This would enable probing of the properties of vertical geometry devices as well.

DATA AVAILABILITY

The data that support the findings of this study are available from the corresponding author upon request.

ACKNOWLEDEGMENTS

We thank Stephane Lorcy for help in sample preparation. The project is supported by ERC grant blackQD (grant n° 756225) and AQDtive (grant n°101086358). We acknowledge the use of clean-room facilities from the “Centrale de Proximité Paris-Centre” and support from Renatech for micro and nanofabrication. This work is supported by Region Ile de France through Sesame project INSIDE. This work is supported by a public grant overseen by the French National Research Agency (ANR) through the grants Frontal (ANR-19-CE09-0017), Copin (ANR-19-CE24-0022), Bright (ANR-21-CE24-0012-02), MixDferro (ANR-21-CE09-0029), Quicktera (ANR-22-CE09-0018), Operatwist (ANR-22-CE09-0037-01), E-map (ANR-23-CE50) and as part of the “Investissements d’Avenir” program (Labex NanoSaclay, reference: ANR-10-LABX-0035). This project has received financial support from the CNRS through the MITI interdisciplinary programs (project WITHIN).

COMPETING INTEREST

The authors declare no competing interests.

Supporting Information

Supporting Information includes (*i*) additional material properties relative to HgTe NCs, (*ii*) procedure for the photoemission map data processing and (*iii*) data relative to PbS NCs and device based on thereof (iv) additional information about device geometry.

DATA AVAILABILITY

The data that support this finding can be obtained from the corresponding author upon reasonable request.

Method

Chemicals. Mercury chloride ($HgCl_2$, Strem Chemicals, 99%), tellurium powder (Te, Sigma-Aldrich, 99.99%), trioctylphosphine (TOP, Alfa aesar, 90%), oleylamine (Acros, 80-90%), dodecanethiol (DDT, Sigma-Aldrich, 98%), lead chloride ($PbCl_2$, Afla Aesar, 99%), sulfur powder (S, Afla Aesar, 99.5%), oleic acid (OA, Afla Aesar, 90%), 1,2-ethanedithiol (EDT, Fluka 98%), 2-mercaptoethanol (MPOH, Merck, >99%), N,N-dimethylformamide (DMF, Sigma Aldrich), ethanol absolute anhydrous (VWR), methanol (Carlo Erba, 99.8%), acetone (VWR), isopropanol (IPA, VWR), n-hexane (VWR), acetonitrile (VWR) and toluene (Carlo Erba, 99.3%).

All chemicals are used as received, except oleylamine which is centrifuged before use. **Mercury and lead salts are toxic, handle them with great care.**

***1 M TOP:Te precursor*.** In a three-neck flask, 6.35 g of Te powder is mixed in 50 mL of TOP. The flask is kept under vacuum at room temperature for 5 min and then is heated up to 100 °C and kept under vacuum for 45 min more. The atmosphere is changed for Ar and the temperature is raised to 275 °C. The solution is stirred until a clear orange coloration is obtained. Then the flask is cooled down and the color switches to yellow. The flask is degassed again for 10 min at room temperature. This solution is finally transferred to a nitrogen-filled glovebox for storage.

***HgTe NCs Synthesis*.** In a 100 mL three-neck flask, 543 mg of $HgCl_2$ and 50 mL of oleylamine (OLA) are degassed from room temperature to 110 °C for an hour. The atmosphere is then switched to nitrogen and the solution is cooled down to 82 °C. A solution of 2 mL of TOP:Te (1 M) and 8 mL of OLA is quickly added to the flask. After 3 minutes, the reaction is quickly quenched by adding a mixture of 1 mL of DDT and 9 mL of toluene. The nanocrystals are precipitated with methanol and redispersed in toluene. Then the nanocrystals are precipitated with ethanol and redispersed in toluene. The solution is centrifuged as is. The pellet is eliminated. Finally, the HgTe colloidal quantum dot solution in toluene is filtered through a 0.2 µm PTFE filter. The obtained solution is used for further characterization and device fabrication.

PbS NCs synthesis: In a three-neck flask, 300 mg of $PbCl_2$ and 7.5 mL of OLA are mixed together and degassed, first at room temperature and then at 110 °C for 30 min. Meanwhile, 30 mg of sulfur powder are mixed with 7.5 mL of OLA until full dissolution and a clear orange solution is obtained.

Then under N_2 at 150 °C, this solution of sulfur is quickly added to the flask. After 15 minutes, the reaction is quickly quenched by addition of 1 mL of oleic acid and 9 mL of hexane. The NCs are precipitated with ethanol and redispersed in hexane. Again, the NCs are precipitated with ethanol and redispersed in hexane and a drop of OA. The cleaning is repeated a third time. Finally, the NCs in toluene are then centrifuged to remove the unstable phase. Finally, the PbS NCs solution is filtered through a 0.2 µm PTFE filter.

HgTe NC film deposition: A ligand exchange solution is prepared with 15 mg of $HgCl_2$ dissolved in 9 mL of DMF, to which 1 mL of MPOH is added. 500 µL of NCs solution (with a concentration of 50 $mg.mL^{-1}$ in chlorobenzene) is mixed with 500 µL of the ligand exchange solution and 5 mL of hexane. Then, 500 µL of DMF is added and the mixture is sonicated and mixed. The NCs undergo a phase transfer from the apolar phase to the DMF phase. The clear apolar phase is discarded using a pipette and two more rounds of cleaning via hexane are performed. Once the apolar phase is removed, the NCs are precipitated by adding a few drops of toluene and centrifuging at 6000 rpm for 3 mins. A pellet forms, which is then redispersed in 200 µL of DMF. Then, the ink is diluted twice in DMF and 8 µL are spin-coated on the sample at 3000 rpm for 150 s to obtain a 50 nm thick film.

PbS NC film deposition: The NCs solution (with an initial concentration of 50 $mg.mL^{-1}$ in toluene) is diluted four times in toluene. In an N_2 filled glovebox, 10 µL of the diluted solution are spin-coated on the sample at 3000 rpm for 30 s. Then, the film is dipped in a solution of EDT 5 mM in acetonitrile for 30 s and rinsed in acetonitrile for 15 s. This yields a film thickness of ≈ 20 nm.

Material characterization

Transmission electron microscopy: A drop of diluted NCs solution is cast on a copper grid covered with an amorphous carbon film. The grid is degassed overnight under secondary vacuum. A JEOL 2010F is used at 200 kV for the acquisition of pictures.

Infrared spectroscopy: A Fischer Nicolet iS50 in attenuated total reflection (ATR) mode is used. The spectra are averaged over 32 acquisitions and have a 4 cm^{-1} resolution.

Electrodes fabrication: The substrate (Si/SiO_2 wafer, 300 nm oxide layer) is cleaned by sonication in acetone bath, then rinsed with acetone and IPA and dried with N_2 gun. Final cleaning is obtained by O_2 plasma. First, the gates are patterned by photolithography. An adhesion primer (TI PRIME) is spin-coated and then baked at 120°C for 2 min. Then, the photoresist (AZ5214E) is spin-coated and baked at 110°C for 90 s before a UV exposure of 1.5 s through the lithography mask. The sample is then baked at 125 °C for 2 min for resist inversion, and flood exposed to UV light for 40 s. Development is carried out for 32 s in AZ726MIF, followed by rinsing in de-ionized water. The sample is plasma cleaned before thermal evaporation of the metal for the electrodes (5nm Ti/40 nm Au). Lift-off is carried out in acetone bath for 30 min. After fabrication of the gate electrodes, 40 nm of Al_2O_3 are deposited by atomic layer deposition (ALD, 450 cycles) to form the gate dielectric. Finally, a second photolithographic process is performed to pattern the source and drain electrodes, this time with the evaporation of 5 nm Ti/80 nm Au.

Photoemission microscopy is conducted on ANTARES beamline of Synchrotron SOLEIL. The synchrotron beam, which is ≈2.5-3 mm wide, is focused using a zone plate (i.e. Fresnel lens), see **Figure 1***a.* The latter is made to operate at low energy (below 100 eV), to obtain optimal focusing. Here, we focus on the Hg 5d state that presents a binding energy around 8 eV, see **Figure 1***c*. In this case, the beam width at the sample position can be down to around 700 nm. The sample is then scanned and the photoelectrons are collected using MBS A-1 hemispherical electron analyzer [77]. The sample holder is moved with step ranging from 500 to 2000 nm typically and for each point we collect a series of photoemission spectra, with a 200 eV pass energy which correspond to a 15.8 eV window with a 17 meV energy step, that are then averaged. Data acquisition lasts from few minutes to one hour depending on the targeted map size. For acquisition with bias applied, we also systematically substrate the grounded map to remove possible charging effect. We used linearly horizontal polarized photons with a photon energy of 95 eV and all measurements were conducted at 240 K, with an energy resolution better than 30 meV. For all maps, angular dispersion of the analyzer (±15°) is neglected by integrating the spectra over all angles. The sample was mounted on the *operando* sample holder of ANTARES beamline equipped with electrical contacts. These electrical contacts, on the side of the sample holder were bonded with gold wires that were connected to the sample pads *via* silver paste. The sample was connected to three Keithley 2450 to apply drain and gates biases.

REFERENCES

[1] Erdem, T. & Demir, H. V. Colloidal Nanocrystals for Quality Lighting and Displays: Milestones and Recent Developments, Nanophotonics **2016**, *5*, 74–95

[2] Beveratos, A.; Kühn, S.; Brouri, R.; Gacoin, T.; Poizat, J.-P. & Grangier, P. Room Temperature Stable Single-Photon Source, Eur. Phys. J. - At. Mol. Opt. Plasma Phys. **2002**, *18*, 191–196

[3] De Vittorio, M.; Pisanello, F.; Martiradonna, L.; Qualtieri, A.; Stomeo, T.; Bramati, A. & Cingolani, R. Recent Advances on Single Photon Sources Based on Single Colloidal Nanocrystals, Opto-Electron. Rev. **2010**, *18*, 1–9

[4] Brokmann, X.; Messin, G.; Desbiolles, P.; Giacobino, E.; Dahan, M. & Hermier, J. P. Colloidal CdSe/ZnS Quantum Dots as Single-Photon Sources, New J. Phys. **2004**, *6*, 99

[5] Pejović, V.; Georgitzikis, E.; Lee, J.; Lieberman, I.; Cheyns, D.; Heremans, P. & Malinowski, P. E. Infrared Colloidal Quantum Dot Image Sensors, IEEE Trans. Electron Devices **2021**, 1–11

[6] Gréboval, C.; Darson, D.; Parahyba, V.; Alchaar, R.; Abadie, C.; Noguier, V.; Ferré, S.; Izquierdo, E.; Khalili, A.; Prado, Y.; et al. Photoconductive Focal Plane Array Based on HgTe Quantum Dots for Fast and Cost-Effective Short-Wave Infrared Imaging, Nanoscale **2022**, *14*, 9359–9368

[7] Soreni-Harari, M.; Yaacobi-Gross, N.; Steiner, D.; Aharoni, A.; Banin, U.; Millo, O. & Tessler, N. Tuning Energetic Levels in Nanocrystal Quantum Dots through Surface Manipulations, Nano Lett. **2008**, *8*, 678–684

[8] Wang, R. The Dynamics of the Peel, Nat. Catal. **2020**, *3*, 333–334

[9] Zhao, H.; Zhu, Y.; Ye, H.; He, Y.; Li, H.; Sun, Y.; Yang, F. & Wang, R. Atomic-Scale Structure Dynamics of Nanocrystals Revealed By In Situ and Environmental Transmission Electron Microscopy, Adv. Mater. **2023**, *35*, 2206911

[10] Zhou, L.; Sun, Y.; Wu, Y.; Zhu, Y.; Xu, Y.; Jia, J.; Wang, F. & Wang, R. Controlled Growth of Pd Nanocrystals by Interface Interaction on Monolayer MoS2: An Atom-Resolved in Situ Study, Nano Lett. **2023**, *23*, 11360–11367

[11] Ye, H.; Zhang, Z. & Wang, R. Nucleation and Growth of Nanocrystals Investigated by In Situ Transmission Electron Microscopy, Small **2023**, *19*, 2303872

[12] Carroll, G. M.; Tsui, E. Y.; Brozek, C. K. & Gamelin, D. R. Spectroelectrochemical Measurement of Surface Electrostatic Contributions to Colloidal CdSe Nanocrystal Redox Potentials, Chem. Mater. **2016**, *28*, 7912–7918

[13] Ravi, V. K.; Markad, G. B. & Nag, A. Band Edge Energies and Excitonic Transition Probabilities of Colloidal CsPbX3 (X= Cl, Br, I) Perovskite Nanocrystals, ACS Energy Lett. **2016**, *1*, 665–671

[14] Chen, M. & Guyot-Sionnest, P. Reversible Electrochemistry of Mercury Chalcogenide Colloidal Quantum Dot Films, ACS Nano **2017**, *11*, 4165–4173

[15] Brown, P. R.; Kim, D.; Lunt, R. R.; Zhao, N.; Bawendi, M. G.; Grossman, J. C. & Bulović, V. Energy Level Modification in Lead Sulfide Quantum Dot Thin Films through Ligand Exchange, ACS Nano **2014**, *8*, 5863–5872

[16] Jagtap, A.; Martinez, B.; Goubet, N.; Chu, A.; Livache, C.; Gréboval, C.; Ramade, J.; Amelot, D.; Trousset, P.; Triboulin, A.; et al. Design of a Unipolar Barrier for a Nanocrystal-Based Short-Wave Infrared Photodiode, ACS Photonics **2018**, *5*, 4569–4576

[17] Chuang, C.-H. M.; Brown, P. R.; Bulović, V. & Bawendi, M. G. Improved Performance and Stability in Quantum Dot Solar Cells through Band Alignment Engineering, Nat. Mater. **2014**, *13*, 796–801

[18] Sarma, D. D.; Santra, P. K.; Mukherjee, S. & Nag, A. X-Ray Photoelectron Spectroscopy: A Unique Tool To Determine the Internal Heterostructure of Nanoparticles, Chem. Mater. **2013**, *25*, 1222–1232

[19] Livache, C.; Izquierdo, E.; Martinez, B.; Dufour, M.; Pierucci, D.; Keuleyan, S.; Cruguel, H.; Becerra, L.; Fave, J. L.; Aubin, H.; et al. Charge Dynamics and Optolectronic Properties in HgTe Colloidal Quantum Wells, Nano Lett. **2017**, *17*, 4067–4074

[20] Greboval, C.; Rastogi, P.; Qu, J.; Chu, A.; Ramade, J.; Khalili, A.; Dabard, C.; Dang, T. H.; Cruguel, H. & Ouerghi, A. Time-Resolved Photoemission to Unveil Electronic Coupling between Absorbing and Transport Layers in a Quantum Dot-Based Solar Cell, J. Phys. Chem. C **2020**, *124*, 23400–23409

[21] Rastogi, P.; Izquierdo, E.; Gréboval, C.; Cavallo, M.; Chu, A.; Dang, T. H.; Khalili, A.; Abadie, C.; Alchaar, R.; Pierini, S.; et al. Extended Short-Wave Photodiode Based on CdSe/HgTe/Ag2Te Stack with High Internal Efficiency, J. Phys. Chem. C **2022**, *126*, 13720–13728

[22] Amelot, D.; Rastogi, P.; Martinez, B.; Gréboval, C.; Livache, C.; Bresciani, F. A.; Qu, J.; Chu, A.; Goyal, M.; Chee, S.-S.; et al. Revealing the Band Structure of FAPI Quantum Dot Film and Its Interfaces with Electron and Hole Transport Layer Using Time Resolved Photoemission, J. Phys. Chem. C **2020**, *124*, 3873–3880

[23] Schneider, C. M.; Wiemann, C.; Patt, M.; Feyer, V.; Plucinski, L.; Krug, I. P.; Escher, M.; Weber, N.; Merkel, M.; Renault, O.; et al. Expanding the View into Complex Material Systems: From

Micro-ARPES to Nanoscale HAXPES, J. Electron Spectrosc. Relat. Phenom. **2012**, *185*, 330–339

[24] Locatelli, A. & Bauer, E. Recent Advances in Chemical and Magnetic Imaging of Surfaces and Interfaces by XPEEM, J. Phys. Condens. Matter **2008**, *20*, 093002

[25] Renault, O. High-Resolution XPS Spectromicroscopy, Surf. Interface Anal. **2010**, *42*, 816–825

[26] Menteş, T. O.; Zamborlini, G.; Sala, A. & Locatelli, A. Cathode Lens Spectromicroscopy: Methodology and Applications, Beilstein J. Nanotechnol. **2014**, *5*, 1873–1886

[27] Locatelli, A.; Aballe, L.; Mentes, T. O.; Kiskinova, M. & Bauer, E. Photoemission Electron Microscopy with Chemical Sensitivity: SPELEEM Methods and Applications, Surf. Interface Anal. **2006**, *38*, 1554–1557

[28] Barrett, N.; Gottlob, D. M.; Mathieu, C.; Lubin, C.; Passicousset, J.; Renault, O. & Martinez, E. Operando X-Ray Photoelectron Emission Microscopy for Studying Forward and Reverse Biased Silicon p-n Junctions, Rev. Sci. Instrum. **2016**, *87*, 053703

[29] Wiemann, C.; Patt, M.; Krug, I. P.; Weber, N. B.; Escher, M.; Merkel, M. & Schneider, C. M. A New Nanospectroscopy Tool with Synchrotron Radiation: NanoESCA@Elettra, E-J. Surf. Sci. Nanotechnol. **2011**, *9*, 395–399

[30] Patt, M.; Wiemann, C.; Weber, N.; Escher, M.; Gloskovskii, A.; Drube, W.; Merkel, M. & Schneider, C. M. Bulk Sensitive Hard X-Ray Photoemission Electron Microscopy, Rev. Sci. Instrum. **2014**, *85*, 113704

[31] Escher, M.; Winkler, K.; Renault, O. & Barrett, N. Applications of High Lateral and Energy Resolution Imaging XPS with a Double Hemispherical Analyser Based Spectromicroscope, J. Electron Spectrosc. Relat. Phenom. **2010**, *178–179*, 303–316

[32] di Mario, L.; Turchini, S.; Zamborlini, G.; Feyer, V.; Tian, L.; Schneider, C. M.; Rubini, S. & Martelli, F. Schottky Barrier Measurements on Individual GaAs Nanowires by X-Ray Photoemission Microscopy, Appl. Surf. Sci. **2016**, *386*, 72–77

[33] Aballe, L.; Foerster, M.; Pellegrin, E.; Nicolas, J. & Ferrer, S. The ALBA Spectroscopic LEEM-PEEM Experimental Station: Layout and Performance, J. Synchrotron Radiat. **2015**, *22*, 745–752

[34] Cavallo, M.; Bossavit, E.; Zhang, H.; Dabard, C.; Dang, T. H.; Khalili, A.; Abadie, C.; Alchaar, R.; Mastrippolito, D.; Prado, Y.; et al. Mapping the Energy Landscape from a Nanocrystal-Based Field Effect Transistor under Operation Using Nanobeam Photoemission Spectroscopy, Nano Lett. **2023**, *23*, 1363–1370

[35] Cavallo, M.; Bossavit, E.; Matzen, S.; Maroutian, T.; Alchaar, R.; Dang, T. H.; Khalili, A.; Dabard, C.; Zhang, H.; Prado, Y.; et al. Coupling Ferroelectric to Colloidal Nanocrystals as Generic Strategy to Engineer the Carrier Density Landscape, Adv. Funct. Mater. **2023**

[36] Cavallo, M.; Ram, A.; Pandey, S.; Maroutian, T.; Bossavit, E.; Ledos, N.; Khalili, A.; Zhang, H.; Prado, Y.; Nguyen, D. L.; et al. Using Wafer Scale Ferroelectric Domains of LiNbO3 to Form Permanent Planar P-n Junction in Narrow Band Gap Nanocrystals, Appl. Phys. Lett. **2023**

[37] Cavallo, M.; Alchaar, R.; Bossavit, E.; Zhang, H.; Dang, T. H.; Khalili, A.; Prado, Y.; Silly, M. G.; Utterback, J. K.; Ithurria, S.; et al. Inside a Nanocrystal-Based Photodiode Using Photoemission Microscopy, Nanoscale **2023**, *15*, 9440–9448

[38] Amati, M.; Barinov, A.; Feyer, V.; Gregoratti, L.; Al-Hada, M.; Locatelli, A.; Mentes, T. O.; Sezen, H.; Schneider, C. M. & Kiskinova, M. Photoelectron Microscopy at Elettra: Recent Advances and Perspectives, J. Electron Spectrosc. Relat. Phenom. **2018**, *224*, 59–67

[39] Zeller, P.; Amati, M.; Sezen, H.; Scardamaglia, M.; Struzzi, C.; Bittencourt, C.; Lantz, G.; Hajlaoui, M.; Papalazarou, E.; Marino, M.; et al. Scanning Photoelectron Spectro-Microscopy: A Modern Tool for the Study of Materials at the Nanoscale, Phys. Status Solidi A **2018**, *215*, 1800308

[40] Wu, C.-L.; Lee, H.-M.; Kuo, C.-T.; Chen, C.-H. & Gwo, S. Absence of Fermi-Level Pinning at Cleaved Nonpolar InN Surfaces, Phys. Rev. Lett. **2008**, *101*, 106803

[41] Avila, J. & Asensio, M. C. First NanoARPES User Facility Available at SOLEIL: An Innovative and Powerful Tool for Studying Advanced Materials, Synchrotron Radiat. News **2014**, *27*, 24–30

[42] Iwasawa, H.; Dudin, P.; Inui, K.; Masui, T.; Kim, T. K.; Cacho, C. & Hoesch, M. Buried Double CuO Chains in YBa 2 Cu 4 O 8 Uncovered by Nano-ARPES, Phys. Rev. B **2019**, *99*, 140510

[43] Kastl, C.; Koch, R. J.; Chen, C. T.; Eichhorn, J.; Ulstrup, S.; Bostwick, A.; Jozwiak, C.; Kuykendall, T. R.; Borys, N. J.; Toma, F. M.; et al. Effects of Defects on Band Structure and Excitons in WS $_2$ Revealed by Nanoscale Photoemission Spectroscopy, ACS Nano **2019**, acsnano.8b06574

[44] Dudin, P.; Lacovig, P.; Fava, C.; Nicolini, E.; Bianco, A.; Cautero, G. & Barinov, A. Angle-Resolved Photoemission Spectroscopy and Imaging with a Submicrometre Probe at the SPECTROMICROSCOPY-3.2L Beamline of Elettra, J. Synchrotron Radiat. **2010**, *17*, 445–450

[45] Koch, R. J.; Jozwiak, C.; Bostwick, A.; Stripe, B.; Cordier, M.; Hussain, Z.; Yun, W. & Rotenberg, E. Nano Focusing of Soft X-Rays by a New Capillary Mirror Optic, Synchrotron Radiat. News **2018**, *31*, 50–52

[46] Gogoi, D.; Wiemann, C.; Dittmann, R. & Schneider, C. M. Resistive Switching Systems: A Spectromicroscopy Approach, Phys. Status Solidi A **2023**, 2300500

[47] Avila, J.; Lorcy, S. & Dudin, P. ANTARES: Space-Resolved Electronic Structure, J. Electron Spectrosc. Relat. Phenom. **2023**, *266*, 147362

[48] Iwasawa, H. High-Resolution Angle-Resolved Photoemission Spectroscopy and Microscopy, Electron. Struct. **2020**, *2*, 043001

[49] Wang, Y. & Dendzik, M. Recent Progress in Angle-Resolved Photoemission Spectroscopy, Meas. Sci. Technol. **2024**, *35*, 042002

[50] Yeh, J.-J. *Atomic Calculation of Photoionization Cross-Sections and Asymmetry Parameters* (Gordon & Breach Science, Publishers, 1993)

[51] Yeh, J. J. & Lindau, I. Atomic Subshell Photoionization Cross Sections and Asymmetry Parameters: $1 \leqslant Z \leqslant 103$, At. Data Nucl. Data Tables **1985**, *32*, 1–155

[52] Gréboval, C.; Chu, A.; Goubet, N.; Livache, C.; Ithurria, S. & Lhuillier, E. Mercury Chalcogenide Quantum Dots: Material Perspective for Device Integration, Chem. Rev. **2021**, *121*, 3627–3700

[53] Tian, Y.; Luo, H.; Chen, M.; Li, C.; Kershaw, S. V.; Zhang, R. & Rogach, A. L. Mercury Chalcogenide Colloidal Quantum Dots for Infrared Photodetection: From Synthesis to Device Applications, Nanoscale **2023**

[54] Lhuillier, E.; Dang, T. H.; Cavallo, M.; Abadie, C.; Khalili, A. & Gréboval, C. in *Handb. II-VI Semicond.-Based Sens. Radiat. Detect. Vol. 1 Mater. Technol.*, edited by G. Korotcenkov (Springer International Publishing, Cham, 2023), pp. 133–156

[55] Buurma, C.; Pimpinella, R. E.; Ciani, A. J.; Feldman, J. S.; Grein, C. H. & Guyot-Sionnest, P. in *Opt. Sens. Imaging Photon Count. Nanostructured Devices Appl. 2016* (SPIE, 2016), p. 993303

[56] Zhang, S.; Bi, C.; Qin, T.; Liu, Y.; Cao, J.; Song, J.; Huo, Y.; Chen, M.; Hao, Q. & Tang, X. Wafer-Scale Fabrication of CMOS-Compatible Trapping-Mode Infrared Imagers with Colloidal Quantum Dots, ACS Photonics **2023**, *10*, 673–682

[57] Luo, Y.; Tan, Y.; Bi, C.; Zhang, S.; Xue, X.; Chen, M.; Hao, Q.; Liu, Y. & Tang, X. Megapixel Large-Format Colloidal Quantum-Dot Infrared Imagers with Resonant-Cavity Enhanced Photoresponse, APL Photonics **2023**, *8*, 056109

[58] Steckel, J. S.; Josse, E.; Pattantyus-Abraham, A. G.; Bidaud, M.; Mortini, B.; Bilgen, H.; Arnaud, O.; Allegret-Maret, S.; Saguin, F.; Mazet, L.; et al. in *2021 IEEE Int. Electron Devices Meet. IEDM* (IEEE, San Francisco, CA, USA, 2021), p. 23.4.1-23.4.4

[59] Pang, C.; Deng, Y.-H.; Kheradmand, E.; Poonkottil, N.; Petit, R.; Elsinger, L.; Detavernier, C.; Geiregat, P.; Hens, Z. & Van Thourhout, D. Integrated PbS Colloidal Quantum Dot Photodiodes on Silicon Nitride Waveguides, ACS Photonics **2023**

[60] Dang, T. H.; Cavallo, M.; Khalili, A.; Dabard, C.; Bossavit, E.; Zhang, H.; Ledos, N.; Prado, Y.; Lafosse, X.; Abadie, C.; et al. Multiresonant Grating to Replace Transparent Conductive Oxide Electrode for Bias Selected Filtering of Infrared Photoresponse, Nano Lett. **2023**, *23*, 8539–8546

[61] Seah, M. P. & Dench, W. A. Quantitative Electron Spectroscopy of Surfaces: A Standard Data Base for Electron Inelastic Mean Free Paths in Solids, Surf. Interface Anal. **1979**, *1*, 2–11

[62] Zhang, H.; Pincelli, T.; Jozwiak, C.; Kondo, T.; Ernstorfer, R.; Sato, T. & Zhou, S. Angle-Resolved Photoemission Spectroscopy, Nat. Rev. Methods Primer **2022**, *2*, 1–22

[63] Radosavljević, M.; Freitag, M.; Thadani, K. V. & Johnson, A. T. Nonvolatile Molecular Memory Elements Based on Ambipolar Nanotube Field Effect Transistors, Nano Lett. **2002**, *2*, 761–764

[64] Song, X.-X.; Zhang, Z.-Z.; You, J.; Liu, D.; Li, H.-O.; Cao, G.; Xiao, M. & Guo, G.-P. Temperature Dependence of Coulomb Oscillations in a Few-Layer Two-Dimensional WS2 Quantum Dot, Sci. Rep. **2015**, *5*, 16113

[65] Gonzalez-Zalba, M. F.; Heiss, D.; Podd, G. & Ferguson, A. J. Tunable Aluminium-Gated Single Electron Transistor on a Doped Silicon-on-Insulator Etched Nanowire, Appl. Phys. Lett. **2012**, *101*, 103504

[66] Dong, Y.; Chen, M.; Yiu, W. K.; Zhu, Q.; Zhou, G.; Kershaw, S. V.; Ke, N.; Wong, C. P.; Rogach, A. L. & Zhao, N. Solution Processed Hybrid Polymer: HgTe Quantum Dot Phototransistor with High Sensitivity and Fast Infrared Response up to 2400 Nm at Room Temperature, Adv. Sci. **2020**, *7*, 2000068

[67] Chen, M.; Lu, H.; Abdelazim, N. M.; Zhu, Y.; Wang, Z.; Ren, W.; Kershaw, S. V.; Rogach, A. L. & Zhao, N. Mercury Telluride Quantum Dot Based Phototransistor Enabling High-Sensitivity Room-Temperature Photodetection at 2000 Nm, ACS Nano **2017**, *11*, 5614–5622

[68] Gréboval, C.; Noumbe, U.; Goubet, N.; Livache, C.; Ramade, J.; Qu, J.; Chu, A.; Martinez, B.; Prado, Y.; Ithurria, S.; et al. Field-Effect Transistor and Photo-Transistor of Narrow-Band-Gap Nanocrystal Arrays Using Ionic Glasses, Nano Lett. **2019**, *19*, 3981–3986

[69] Gréboval, C.; Chu, A.; Magalhaes, D. V.; Ramade, J.; Qu, J.; Rastogi, P.; Khalili, A.; Chee, S.-S.; Aubin, H.; Vincent, G.; et al. Ferroelectric Gating of Narrow Band-Gap Nanocrystal Arrays with Enhanced Light–Matter Coupling, ACS Photonics **2021**, *8*, 259–268

[70] Chee, S.-S.; Gréboval, C.; Magalhaes, D. V.; Ramade, J.; Chu, A.; Qu, J.; Rastogi, P.; Khalili, A.; Dang, T. H.; Dabard, C.; et al. Correlating Structure and Detection Properties in HgTe Nanocrystal Films, Nano Lett. **2021**, *21*, 4145–4151

[71] Qin, T.; Mu, G.; Zhao, P.; Tan, Y.; Liu, Y.; Zhang, S.; Luo, Y.; Hao, Q.; Chen, M. & Tang, X. Mercury Telluride Colloidal Quantum-Dot Focal Plane Array with Planar p-n Junctions Enabled by in Situ Electric Field–Activated Doping, Sci. Adv. **2023**, *9*, eadg7827

[72] Dunfield, S. P.; Bojar, A.; Cacovich, S.; Frégnaux, M.; Klein, T.; Bramante, R.; Zhang, F.; Regaldo, D.; Dufoulon, V.; Puel, J.-B.; et al. Carrier Gradients and the Role of Charge Selective Contacts in Lateral Heterojunction All Back Contact Perovskite Solar Cells, Cell Rep. Phys. Sci. **2021**, *2*, 100520

[73] Zhang, H.; Ledos, N.; Cavallo, M.; Bossavit, E.; Khalili, A.; Curti, L.; Xu, X. Z.; Dandeu, E.; Utterback, J. K.; Ithurria, S.; et al. Photoemission Insight on Narrow Band Gap PbS Quantum Dots Relevant for Infrared Imaging, J. Phys. Chem. C **2024**, *128*, 2028–2036

[74] Gréboval, C.; Izquierdo, E.; Abadie, C.; Khalili, A.; Cavallo, M.; Chu, A.; Dang, T. H.; Zhang, H.; Lafosse, X.; Rosticher, M.; et al. HgTe Nanocrystal-Based Photodiode for Extended Short-Wave Infrared Sensing with Optimized Electron Extraction and Injection, ACS Appl. Nano Mater. **2022**, *5*, 8602–8611

[75] Ackerman, M. M.; Tang, X. & Guyot-Sionnest, P. Fast and Sensitive Colloidal Quantum Dot Mid-Wave Infrared Photodetectors, ACS Nano **2018**, *12*, 7264–7271

[76] Khalili, A.; Cavallo, M.; Bossavit, E.; Alchaar, R.; Dang, T. H.; Dabard, C.; Zhang, H.; Ledos, N.; Parahyba, V.; Potet, P.; et al. In Situ Mapping of the Vectorial Electric Field within a Nanocrystal-Based Focal Plane Array Using Photoemission Microscopy, ACS Appl. Electron. Mater. **2023**, *5*, 4377–4384

[77] Avila, J.; Razado-Colambo, I.; Lorcy, S.; Lagarde, B.; Giorgetta, J.-L.; Polack, F. & Asensio, M. C. ANTARES, a Scanning Photoemission Microscopy Beamline at SOLEIL, J. Phys. Conf. Ser. **2013**, *425*, 192023

TOC Graphic

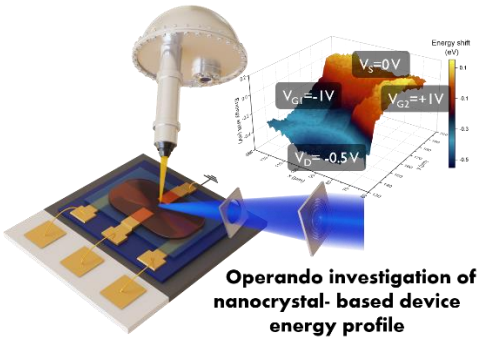
Energy shift (eV)
V_S=0 V
V_{G1}=-1V
V_{G2}=+1V
V_D= -0.5 V
Operando investigation of nanocrystal- based device energy profile

Supporting information for

Operando Investigation of Nanocrystal based Device Energy Landscape: Seeing the Current Pathway

Mariarosa Cavallo[1], Dario Mastrippolito[1], Erwan Bossavit[1], Leonardo Curti[2], Adrien Khalili[1], Huichen Zhang[1], Nicolas Ledos[1], Yoann Prado[1], Erwan Dandeu[1], Michael Rosticher[3], Sandrine Ithurria[2], Pavel Dudin[4], José Avila[4*], Debora Pierucci[1], Emmanuel Lhuillier[1*]

[1] Sorbonne Université, CNRS, Institut des NanoSciences de Paris, 4 place Jussieu, 75005 Paris, France.
[2] Laboratoire de Physique et d'Etude des Matériaux, ESPCI, PSL Research University, Sorbonne Université, CNRS, 10 rue Vauquelin, 75005 Paris, France.
[3] Laboratoire de physique de l'Ecole Normale Supérieure, ENS, Université PSL, CNRS, Sorbonne Université, Université Paris Cité, 24 Rue Lhomond, 75005 Paris, France
[4] Synchrotron SOLEIL, L'Orme des Merisiers, Départementale 128, 91190 Saint-Aubin, France.

*To whom correspondence should be sent: el@insp.upmc.fr, jose.avila@synchrotron-soleil.fr

Table of content

1. Material characterization of the HgTe NCs.

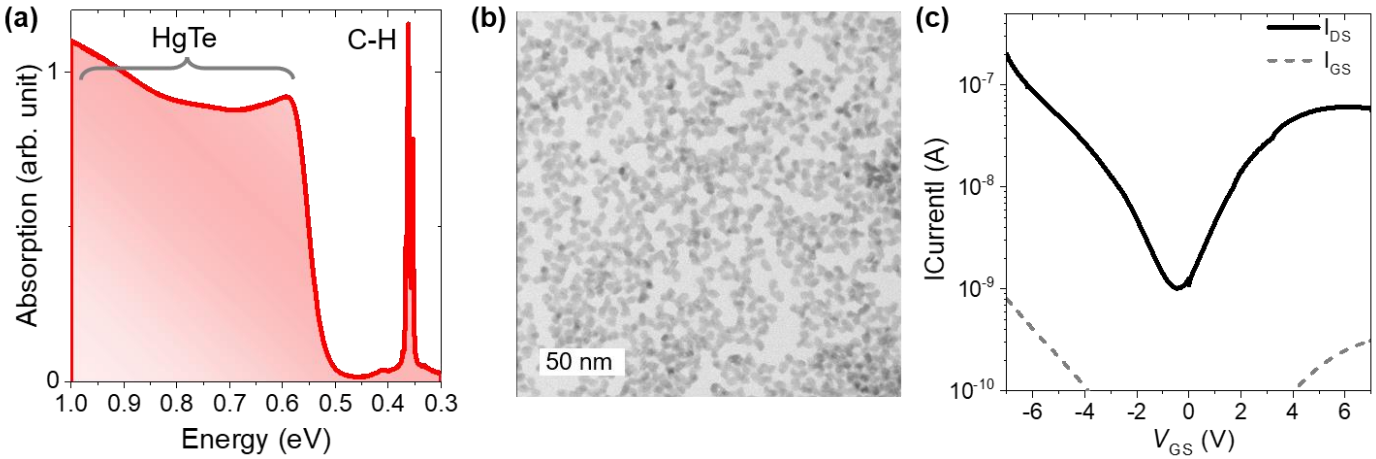

Figure S 1 Properties of the HgTe NCs*. a. absorption spectrum for HgTe NCs with a 0.5 eV cut-off energy. b. TEM image of HgTe NCs with a 0.5 eV cut-off energy. c. Transfer curve (drain and gate current as a function of applied gate bias) for field-effect transistor (HgTe NCs as channel) displaying an ambipolar character.*

2. Procedure for the processing of the raw photoemission data

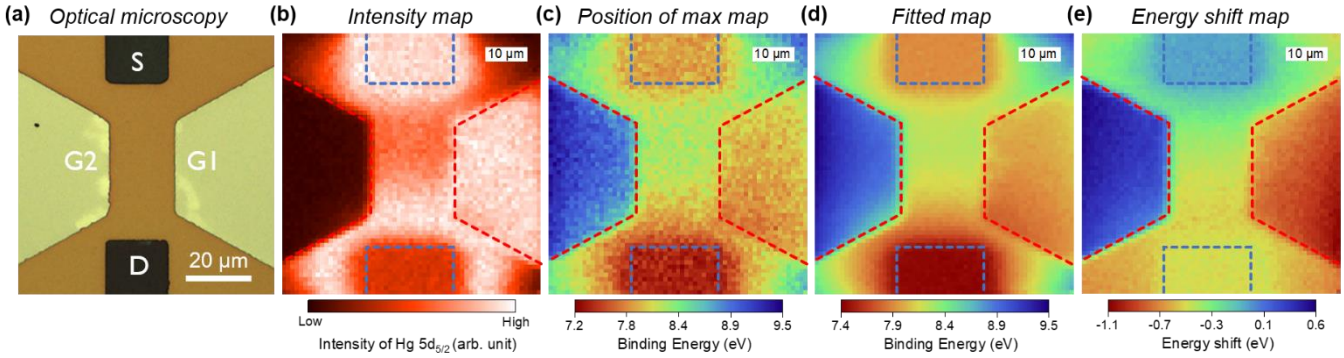

Figure S 2 Processing procedure of the photoemission map*. a. Optical microscopy image of the dual gated transistor. b. Intensity map of the same area. c. Map displaying the energy for the Hg 5d state maximum of intensity. d. Binding energy map obtained by fitting the Hg 5d state. e. Energy shift map obtained by subtracting the previous map from its equivalent map while all electrodes are grounded. This procedure enables the removal of the charging effect.*

3. Procedure for the processing of the raw photoemission data

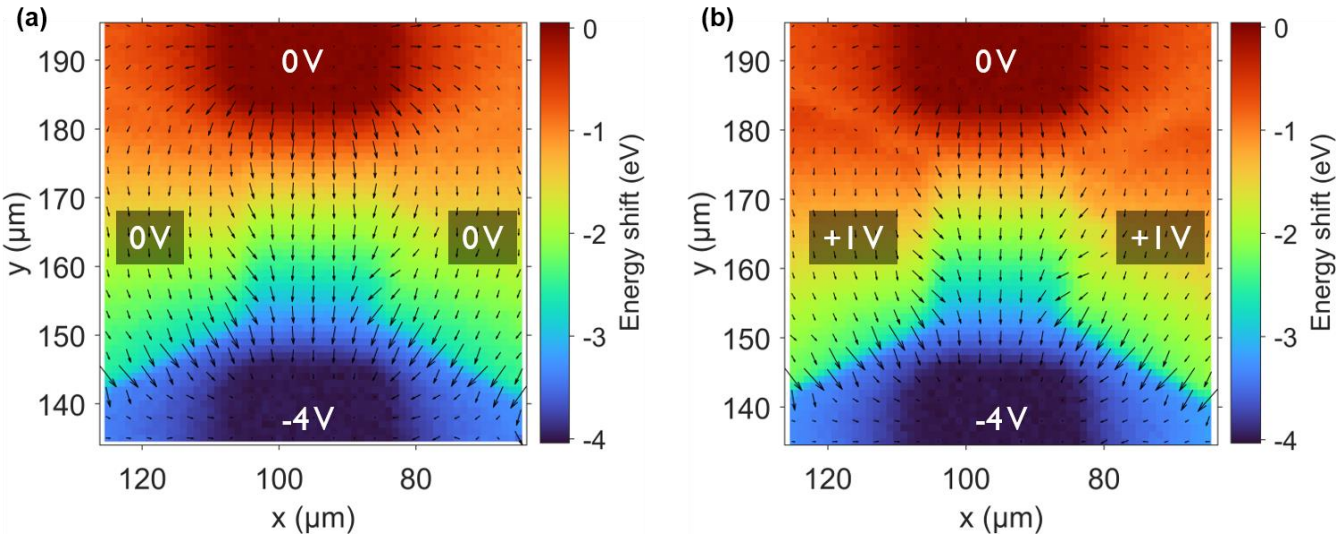

Figure S 3 Vectorial mapping on dual gate device. *a (resp b.) are superposition of the energy shift map (color map) and electric field map for the dual gate FET in which the field direction and magnitude are given by the arrow for each position, while V_{DS}=-4 V and V_{GS}=0 V (resp. V_{GS}=+1 V)*

4. Data for FET based on PbS NCs channel

Figure S 4~~Figure S 4~~~~Figure S 3~~ displays the physical properties of the PbS NCs. Their size is around 8 nm according to TEM (Figure S 4~~Figure S 4~~~~Figure S 3~~a). Their band gap is around 0.7 eV (Figure S 4~~Figure S 4~~~~Figure S 3~~b). The static non-spatially resolved photoemission spectra of the material are given in Figure S 4~~Figure S 4~~~~Figure S 3~~c-f.

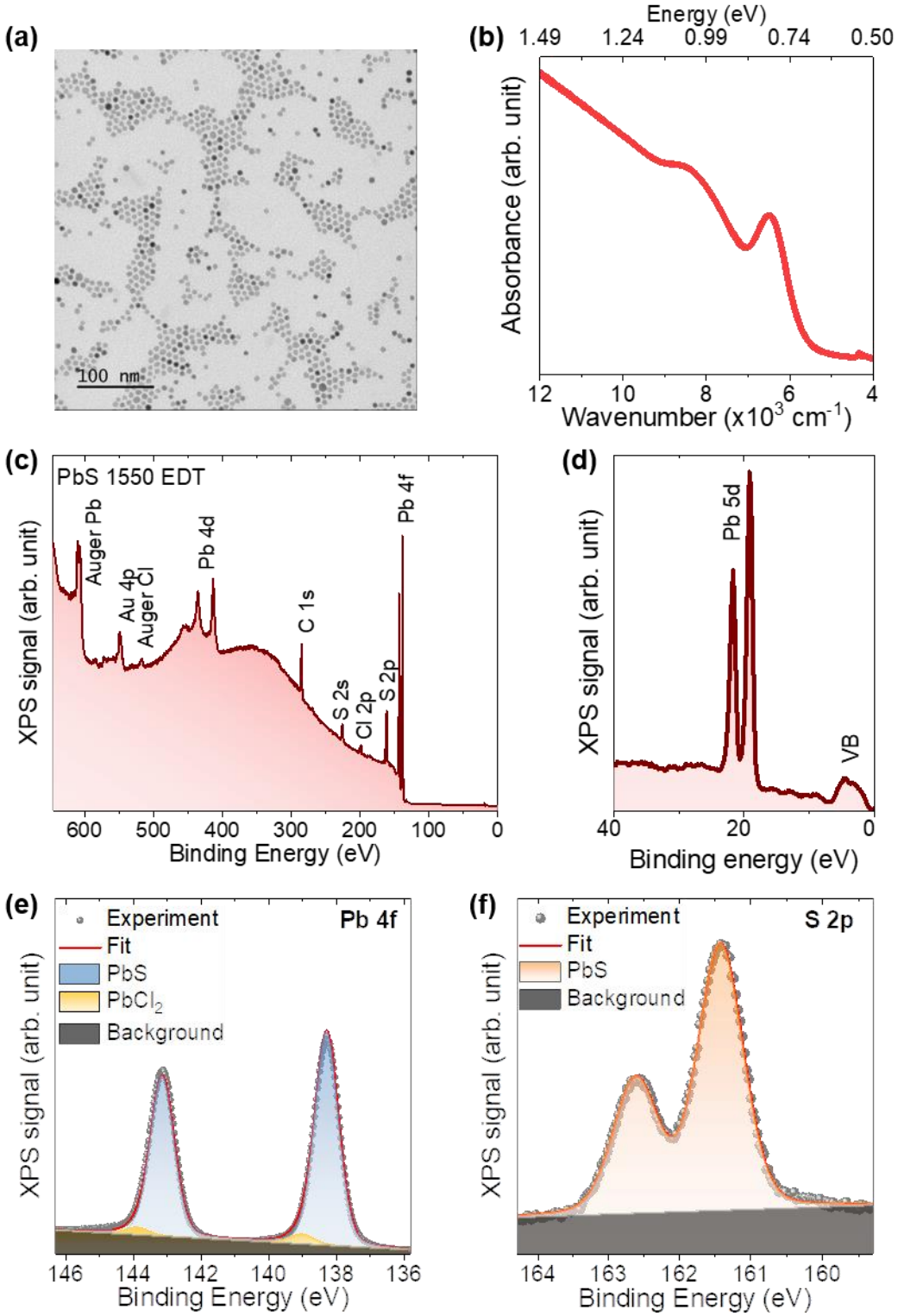

Figure S 4 Physical properties of PbS NCs with a 1550 nm band edge*. a TEM image for the PbS NCs. b. Absorption spectrum for the PbS NCs. c. Photoemission survey spectrum acquired for hv=700 eV for a PbS NC film capped with EDT ligands. d. Photoemission spectrum of the Pb 5d state. e. Photoemission spectrum of the Pb 4f state. f. Photoemission spectrum of the S 2p state.*

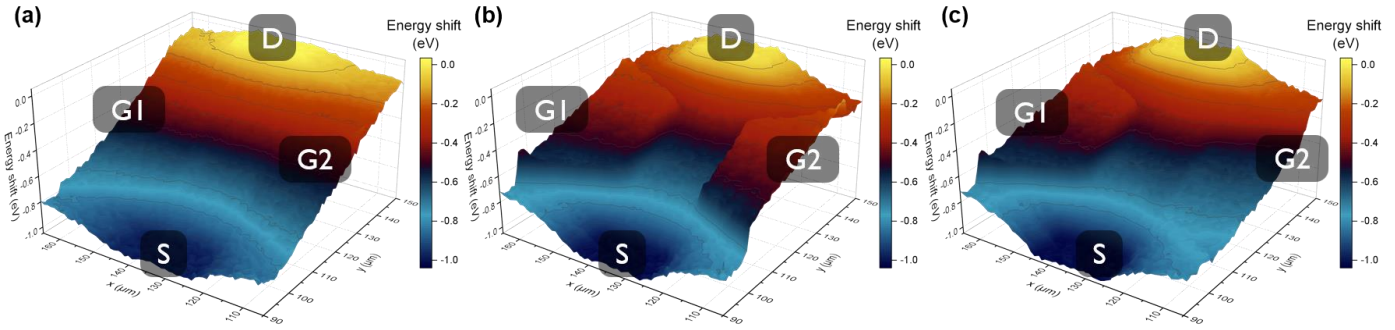

Figure S 5 Operando 3D mapping of the FET energy landscape with PbS NCs channel *. a, b and c are respectively energy shift maps for the single gated device for V_{DS}=-1 V, V_{GS}=0 V ; V_{DS}=-1 V, V_{G1}= V_{G2}=+4 V and V_{DS}=-1 V, V_{G1}= -V_{G2}=+4 V.*

5. Geometry for other devices

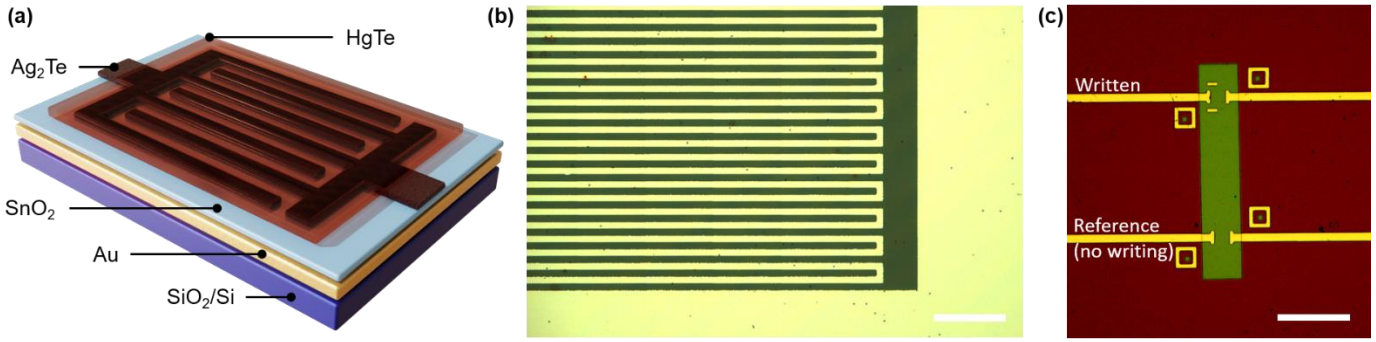

Figure S 6 Geometrical device from Figure 5. *a. Sschematic of the planar p-n junction. b. Optical microscopy image of the Ag_2Te pattern deposited onto SnO_2 layer deposited on gold layer. c. Optical microscopy image for the nanocrystal film coupled to a PZT ferroelectric layer (in green), whereas the red background correspond to SiN. Scale bars in the optical images correspond to 100 µm.*